Sensors & Actuators: B. Chemical 333 (2021) 129570

Contents lists available at ScienceDirect

Sensors and Actuators: B. Chemical

journal homepage: www.elsevier.com/locate/snb

Electrochemical nanobiosensor for early detection of rheumatoid arthritis biomarker: Anti- cyclic citrullinated peptide antibodies based on polyaniline (PANI)/MoS_2-modified screen-printed electrode with PANI-Au nanomatrix-based signal amplification

Sathish Panneer Selvam [a], Somasekhar R. Chinnadayyala [a,*], Sungbo Cho [a,b,**]

[a] Department of Electronic Engineering, Gachon University, Seongnam-si, Gyeonggi-do, 13210, Republic of Korea
[b] Gachon Advanced Institute for Health Science & Technology, Gachon University, Incheon, 21999, Republic of Korea

ARTICLE INFO

Keywords:
Anti-cyclic citrullinated peptide antibodies
Rheumatoid arthritis
Biosensor
Square wave voltammetry
Electrochemical impedance spectroscopy
Human serum

ABSTRACT

Anti-cyclic citrullinated peptide (aCCP) antibodies are predictive biomarker tools for early detection of rheumatoid arthritis. In this study, square wave voltammetry (SWV) electrochemical aCCP immunosensor was fabricated using molybdenum disulfide (MoS_2) polyaniline (PANI) as the base matrix of the screen-printed electrode (SPE) while employing an interfacial polymerized PANI-gold (Au) nanomatrix to entrap the aCCP antibodies with higher signal amplification. The modified electrode was characterized morphologically by Scanning electron microscopy, Transmission electron microscopy, X-ray photoelectron spectroscopy, Fourier-transform–Infrared spectroscopy (FT-IR), UV–vis spectroscopy, X-ray diffraction and electrochemically by Electrochemical impedance spectroscopy, Cyclic voltammetry and Square wave voltammetry. The sensor performance was investigated in 1X phosphate-buffered saline (PBS) and human serum (10 % HS), where the obtained limit of detection values was 0.16 IU/mL (PBS) and 0.22 IU/mL (10 % HS) with logarithmic linearity between 0.25 and 1500.0 IU/mL of aCCP. The sensor showed selectivity, storage stability (7.7 % lost after 4 weeks), repeatability (3.32 % RSD) and reproducibility (3.49 % RSD). The immunosensor was also applied to real-time aCCP detection in aCCP-spiked HS.

1. Introduction

Rheumatoid arthritis (RA) is a chronic autoimmune disease that produces a progressive inflammatory response that leads to severe pain, swelling, and stiffness in the joints of hands and feet, followed by occurrence of irreversible damage. It has been reported that 1% of the world's population is affected by RA [1–3]. The exact cause for the generation of autoimmune antibodies is still unknown, but it is believed that the triggering mechanism caused by genetic (HLA-DR1 and HLA-DR4) and environmental (smoking and pathogens) factors producing autoimmune antibodies attack their own cells [4,5]. In brief, citrullination of peptides in Type-II collagen and vimentin produces citrulline in the place of arginine [6]. Meanwhile, the production of IgM Rheumatoid factor (RF) and aCCP antibodies produces immune complexes with specific antigens that accumulate at the inflamed joints. According to the ACE criteria, RF is the only marker that can be serologically tested for the clinical manifestation of RA. However, as RF also is found in other types of rheumatic and non-rheumatic diseases, the specificity of RF for RA detection is poor. Specifically, if the RF factor test yields positive results, a confirmatory aCCP test is required to rule out other types of rheumatic disease from RA. Early detection of RA indeed plays a vital role in preventing irreversible joint erosion. Almost 70 % of the people with a positive anti-CCP antibody in their serum have a 5-year risk of developing RA; this is plentiful for clinical intervention of RA treatment [7]. The impact of anti-rheumatic therapy can be assessed by evaluating the level of aCCP along with RF factor [8–10]. Furthermore, because of the early presence of aCCP autoantibodies and their higher specificity, aCCP antibodies can serve as superior diagnostic markers in the early detection of RA. The normal level of aCCP is considered to be <20 IU/mL and the cut-off values of aCCP antibody

* Corresponding author.
** Corresponding author at: Department of Electronic Engineering, Gachon University, Seongnam-si, Gyeonggi-do, 13210, Republic of Korea.
E-mail addresses: ssreddy@gachon.ac.kr (S.R. Chinnadayyala), sbcho@gachon.ac.kr (S. Cho).

https://doi.org/10.1016/j.snb.2021.129570
Received 19 November 2020; Received in revised form 9 January 2021; Accepted 25 January 2021
Available online 1 February 2021
0925-4005/© 2021 Elsevier B.V. All rights reserved.

level have been set at 20 IU/mL for RA.

For the detection of aCCP antibodies, citrullinated vimentin, citrullinated a-enolase, and citrullinated fibrinogen can be used as the discerning antigens for diagnosing RA. Cyclic citrullinated peptides (CCPs) are the most common selective antigens for recognizing aCCP antibodies [11,12]. Present day diagnostic techniques for aCCP antibody detection include enzyme-linked immunosorbent assay (ELISA) [13,14], surface-enhanced Raman scattering [15,16], chemiluminescence analysis [17,18], fluorescence-based analysis [19] and electrochemical analysis. ELISA requires extended incubation time, large sample volume and the number of intermediate sample preparation steps are more. A highly reliable system is required for Surface-enhanced Raman scattering based sensing methods and an expensive technique. Chemiluminescence and fluorescence-based detection methods are expensive, limited to a certain application, time-consuming and less compatibility. Though conventional analytical methods are available, among the aforementioned aCCP detection methods, electroanalytical based immunodetection methods require a low volume of sample, higher sensitivity, inexpensive technique, no skilled operator required and electrochemical sensors can be developed portably [20,21]. These are the reasons make electrochemical sensors to be unique and superior to other techniques. CCP-coated microtiter plates and horseradish peroxidase (HRP)-labeled IgG antibodies are used in ELISA assays to detect aCCP antibodies. The commercially developed aCCP ELISA assay kit 31-K01 (https://eaglebio.com/wp-contentuploads/datapdf/ccp31-k01-anti-ccp-elisa-assay-kit-package-insert.pdf) from Eagle Biosciences Inc. provides a non-linear range between 1 and 2000 IU/mL with a logarithmic calibration plot. Guerrero et al. developed an electrochemical sensor based on neutravidin-functionalized magnetic microbeads-modified screen-printed electrode (SPE) for aCCP detection in human serum, where a linear dynamic range of 10–1000 IU/mL with a limit of detection (LOD) of 2.5 IU/mL for aCCP was reported [11]. An increase in the titer concentration of aCCP antibodies can serve as a predictive tool for RA and provide therapeutic information about the effectiveness of the treatment. Thus, accurate quantification of aCCP antibodies in human serum within the desired dynamic range, with a higher detection limit, and with precise selectivity toward aCCP antibodies should be demonstrated appropriately.

Progressive development of nanotechnology ushers in new prospects for electrochemical sensors. Specifically, electroanalysis of biomarker detection using differential pulse voltammetry, SWV, and chronoamperometry can be an appropriate solution for clinical diagnosis [11,22–24]. The development of a nanostructured matrix to increase the loading capacity of analytes and to amplify the electrochemical signal plays a vital role in the enhancement of detection sensitivity. A wide range of nanomaterials have been used in the construction of immunosensors to amplify their electrochemical performance, including metal-based nanomaterials and conductive polymers [25–28]. On one hand, under the conductive polymer category, polyaniline (PANI) is a widely studied nanostructured matrix because of its durability and because nanoparticles can be easily incorporated into the PANI matrix. On the other hand, Au nanoparticles (Au NPs) have gained much attention for developing electrochemical sensing base matrices and signal amplifiers because of their high conductivity and biocompatibility in the sensitive electrochemical detection of biological molecules [29–31]. 2D transition metal dichalcogenide sheets are widely employed to enhance the electrocatalytic activity of the sensing platform because of their high conductivity, inherent electrochemical activity, and simple synthesis procedure [32]. Specifically, MoS_2 possesses excellent conductivity and functionalization of MoS_2 with conductive polymers could be an inevitable approach as it allows for a great improvement in the solubility of MoS_2 [33,34].

In this report, carbon-based microvolume operating SPE was utilized as a base electrode. Initially, the SPE surface was modified with MoS_2 ink, owing to its high electrocatalytic activity. A fine PANI layer was electrodeposited on MoS_2/SPE to enhance the conductivity and cohesive behavior of the electrode, which can prevent the electrode material from being leached off. Furthermore, upon immobilization of the recognition element (CCP) through N-(3-dimethylaminopropyl)-N-ethylcarbodiimide hydrochloride and N-hydroxysulfosuccinimide (EDC-NHS) chemistry, PANI was able to form a stable amide bond with CCP because of its amine group (Scheme 2). Subsequently, the PANI nanowire-Au NP nanomatrix, which was used as a nanomatrix probe for entrapping aCCP antibodies with higher loading capacity through physical adsorption and electrostatic interaction between Au NPs and aCCP antibodies (Scheme 1b). The CV and EIS results suggest the importance of PANI-Au nanomatrix and the SPE surface modification with MoS_2/PANI in microvolume operating aCCP sensor. The schematic representation of the SPE electrode at major stages of the surface modification is shown in Scheme 1a and supplementary movie.

2. Experimental

2.1. Reagents and apparatus

Refer supplementary information (S1) for reagents and apparatus section.

2.2. Synthesis of Au-PANI nanomatrix

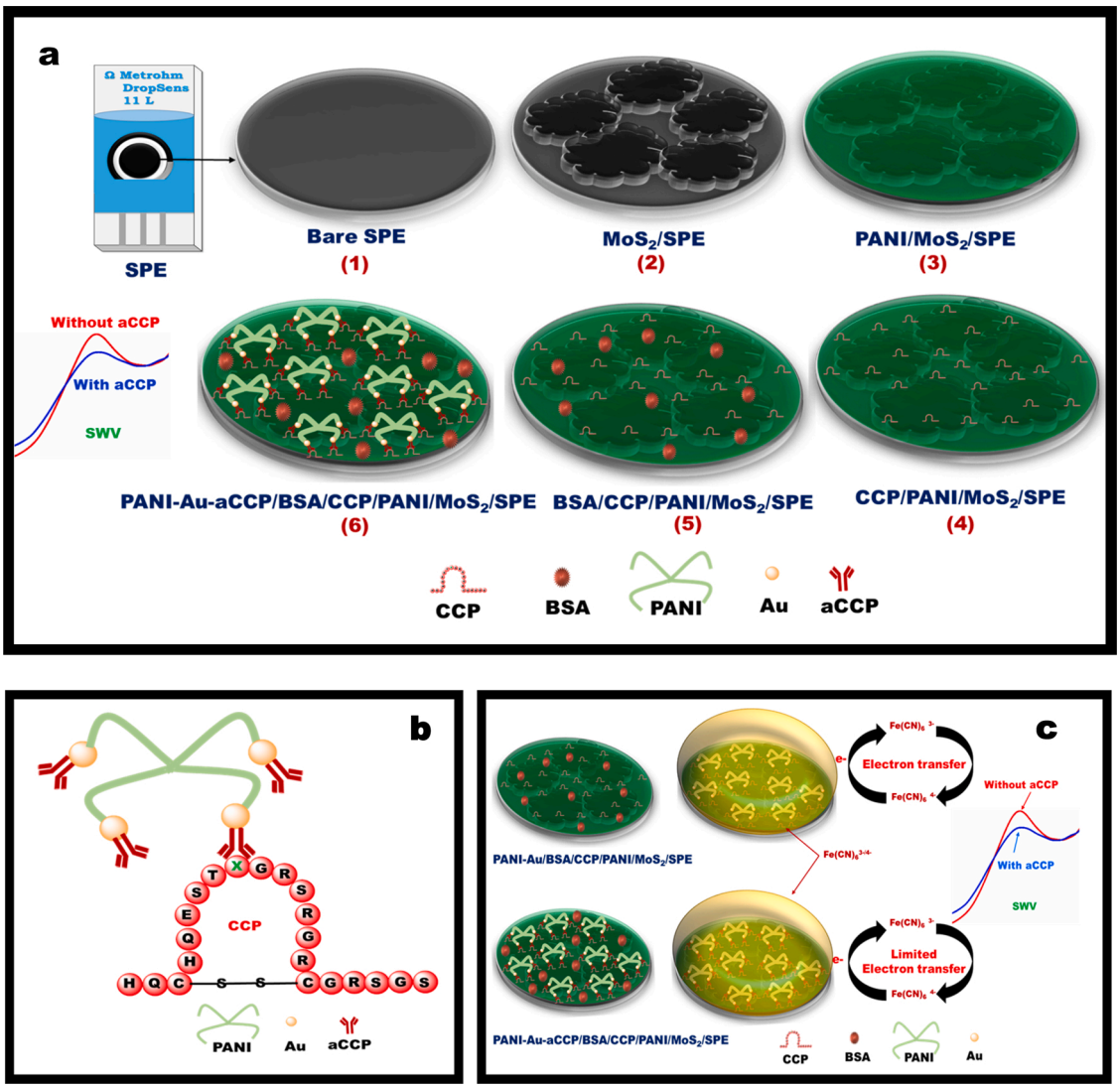
The interfacial polymerization method of synthesis was employed to produce the PANI-Au nanocomposite. By introducing an aqueous solution containing 3 mM $HAuCl_4$ in 0.1 M HCl into 0.5 M aniline in toluene (organic phase), the interfacial polymerization process was initiated and PANI nanofibers were formed slowly in the aqueous phase of the solution. At the same time, Au NPs were also synthesized and incorporated into the PANI nanofibers during the polymerization process [35]. The prepared PANI-Au solution was centrifuged at room temperature and diffused three times through Milli-Q water for purification. The purified PANI-Au solution was stored at 4 °C until further use.

2.3. Preparation of PANI-Au-aCCP

To construct a standard calibration curve, the fabricated immunosensor was calibrated with seven different concentrations of aCCP; the calibration standards were denoted in IU/mL, as per the World Health Organization standard reference for RA. 5.0 μL of the prepared PANI-Au nanoprobe was mixed with aCCP under shaking conditions for 1 h, followed by addition of 0.5 % BSA to block the remaining active sites on the PANI-Au nanoprobe. PANI-Au-aCCP was then incubated at 4 °C for 1 h.

2.4. Construction of PANI/MoS_2-modified SPEs

MoS_2 NS (5 mg) was dispersed in 1 mL of isopropyl alcohol; 50 μL of Nafion was added to this to enhance the cohesive characteristics of MoS_2 toward the electrode surface. The prepared solution was sonicated using a probe at 45 % amplitude for 5 min. About 10 μL of prepared MoS_2 ink was dropped onto SPE to achieve the preferred catalyst loading of 50 μg (≈398.1 μg/cm^2) [36]. To enhance the electrochemical performance of the MoS_2/SPE electroactive matrix, a fine PANI thin film layer was electrochemically deposited on MoS_2/SPE. Electrochemical polymerization of aniline was carried out in 1 M HCl containing 0.1 M aniline at the potential range between -0.4 to 1.0 V for 10 cycles [37]. The redox conversion of leucoemeraldine to emeraldine and emeraldine to pernigraniline was identified in the corresponding characteristic peaks at potentials of 0.25, 0.54, and 0.92 V (Fig. 1i). Electropolymerized PANI-modified MoS_2/SPE was washed with running Milli-Q water to remove the inactive adsorbed aniline monomer at the electrode surface. Since electrosynthesized PANI is a porous material, it possesses a high degree of adhesive tendency compared with bare SPE. Thus, it can easily be entrapped on MoS_2/SPE strongly. Moreover, the electrostatic



Scheme 1. (a) Schematic representation for the fabrication of PANI-Au aCCP/BSA/CCP/PANI/MoS_2/SPE for sensitive detection of aCCP, (b) Schematic representation of the interaction between CCP and aCCP antibodies bound PANI-Au nanomatrix (X = Citrulline), (c) Mechanism of aCCP immunosensor in the detection of aCCP using $Fe(CN)_6^{3-}/^{4-}$ as a mediator.

interaction between the positive charge-containing PANI and the negative charge-containing MoS_2 nanosheets results in a strong interaction between MoS_2 and the PANI layer.

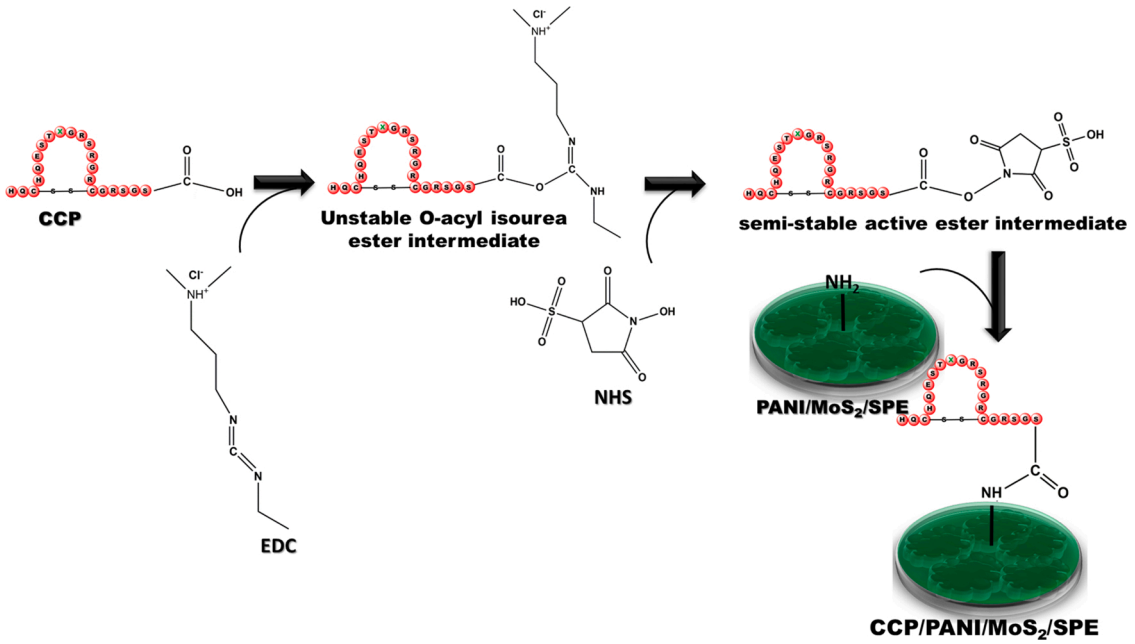
2.5. Fabrication of BSA/CCP/PANI/MoS_2/SPEs

Selection of the biological recognition mechanism is crucial in the fabrication of a biosensor. Thus, citrulline-containing cyclic filaggrin peptide (21-mer) was employed explicitly to recognize the aCCP antibodies. EDC-NHS surface chemistry was employed to immobilize CCP onto PANI/MoS_2/SPE. The carboxyl functional group of the CCP (100 μg/mL in 1X PBS) was allowed to react with EDC (0.4 M) to form an unstable amine-reactive O-acyl isourea ester intermediate under stirring for 30 min. When 0.1 M sulfo-NHS was added to the above-synthesized solution, NHS attached to the carboxyl group of the CCP and caused the formation of a semi-stable active ester intermediate (Scheme 2) [38]. Eventually, when the above-prepared solution was dropped on the PANI/MoS_2/SPE, the amine group in PANI facilitated the formation of a stable amide bond with CCP. To avoid exposure of the active sites at the PANI/MoS_2/SPE, 5.0 μL of 0.5 % bovine serum albumin (BSA) was dropped onto CCP/PANI/MoS_2/SPE and incubated at 4 °C. After incubation, the fabricated BSA/CCP/PANI/MoS_2/SPE was gently rinsed twice with 10 μL of 1X PBS.

3. Results and discussion

3.1. Characterization of PANI/MoS_2 and PANI-Au

The scanning electron microscopy (SEM) was employed to confirm the structural characterization of the surface-modified SPEs and to study the differences in the individual layers of the surface-modified SPEs. First, bare SPE contains higher surface roughness because of the nature of carbon (Fig. 1a). After MoS_2 ink was dropped onto SPE, the presence of MoS_2 nanosheets was clearly observed in MoS_2/SPE, in addition to the observation of the sheet-like characteristics of MoS_2 (Fig. 1b). The electropolymerized PANI layer on MoS_2/SPE clear showed a nanowire structured PANI in Fig. 1c. A cross-sectional SEM image of PANI/MoS_2/SPE distinguished the individual MoS_2 nanosheets and the electrodeposited PANI layer (Fig. S3a and b). Fig. 1d shows the Au NP-embedded PANI nanowire matrix. Elemental dispersive X-ray and elemental mapping analysis confirmed the presence of individual elements such as C, N, Cl, Mo, and S in the PANI/MoS_2 sample (Fig. S1a-f), and C, N, Cl, and Au in the PANI-Au nanomatrix (Fig. S2a-e). Morphological and structural investigations of the MoS_2 nanosheets and the



Scheme 2. Immobilization of CCP through EDC-NHS surface chemistry on PANI/MoS_2/SPE.

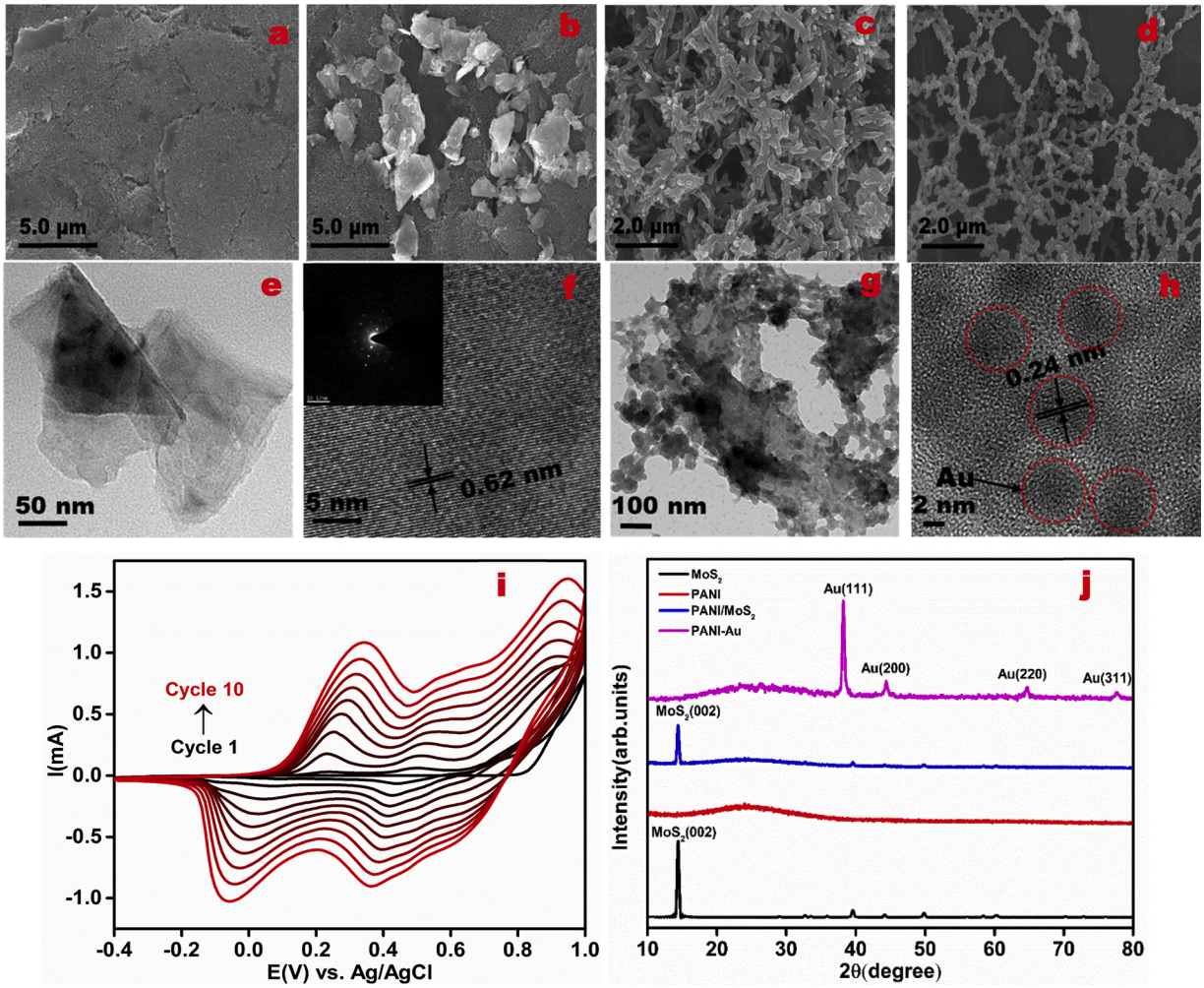


Fig. 1. SEM images of (a) bare SPE, (b) MoS_2/SPE, (c) PANI/MoS_2/SPE, and (d) PANI-Au nanomatrix, (e) TEM image of MoS_2, (f) lattice fringe image of MoS_2 (the inset image displays SAED pattern of MoS_2), (g) TEM image of PANI-Au, and (h) HR-TEM image of Au within the PANI nanowire, (i) CV response of electrodeposition of PANI from 10 cycles of CV at 50 mV/s scan rate in the presence of 0.1 M aniline in 1 M HCl, (j) XRD pattern of MoS_2, PANI, PANI/MoS_2, and PANI-Au.

PANI-Au nanomatrix were carried out using transmission electron microscopy (TEM) analysis. Fig. 1e shows a very thin sheet-like well-crystallized 2D structure of MoS_2 nanosheets. In the inset image, the hexagonal lattice and characteristic lattice fringes (0.62 nm) confirmed the presence of the (002) plane of MoS_2 [39,40] (Fig. 1f). A high amount of Au NP-loaded PANI nanowires can be seen in Fig. 1g, where the size range of the dispersed Au NPs within the PANI nanowire was approximately 6−14 nm. The presence of large amounts of Au NPs within PANI can facilitate the entrapment of large quantities of aCCP antibodies through electrostatic interactions. The high resolution (HR)-TEM image (Fig. 1h) confirmed the presence of Au NPs with a lattice fringe of 0.24 nm [41].

X-ray diffraction (XRD) analysis was carried out to analyze the crystalline phase of the MoS_2, PANI, PANI/MoS_2, and PANI-Au layers (Fig. 1j). The presence of a strong characteristic peak at 14.4° for the MoS_2 nanosheet confirmed good crystallinity of the MoS_2 nanosheets; the characteristic reflection peak of MoS_2 (002) was indexed based on the ICDD 77-1716 reference pattern [42]. In the electropolymerized PANI sample, a broad peak was observed at 24°, which represents the amorphous characteristics of PANI [43]. The PANI/MoS_2 XRD pattern displayed characteristic peaks of MoS_2 (14.4°) and PANI (24.0°). This confirms that there was no change in the crystalline phase during the electropolymerization of PANI on the MoS_2 layer, confirming the existence of PANI and MoS_2 in the PANI/MoS_2 nanocomposite layer. The interfacial polymerized PANI-Au sample showed a broad amorphous characteristic peak of PANI at 24.9° and based on the ICDD reference

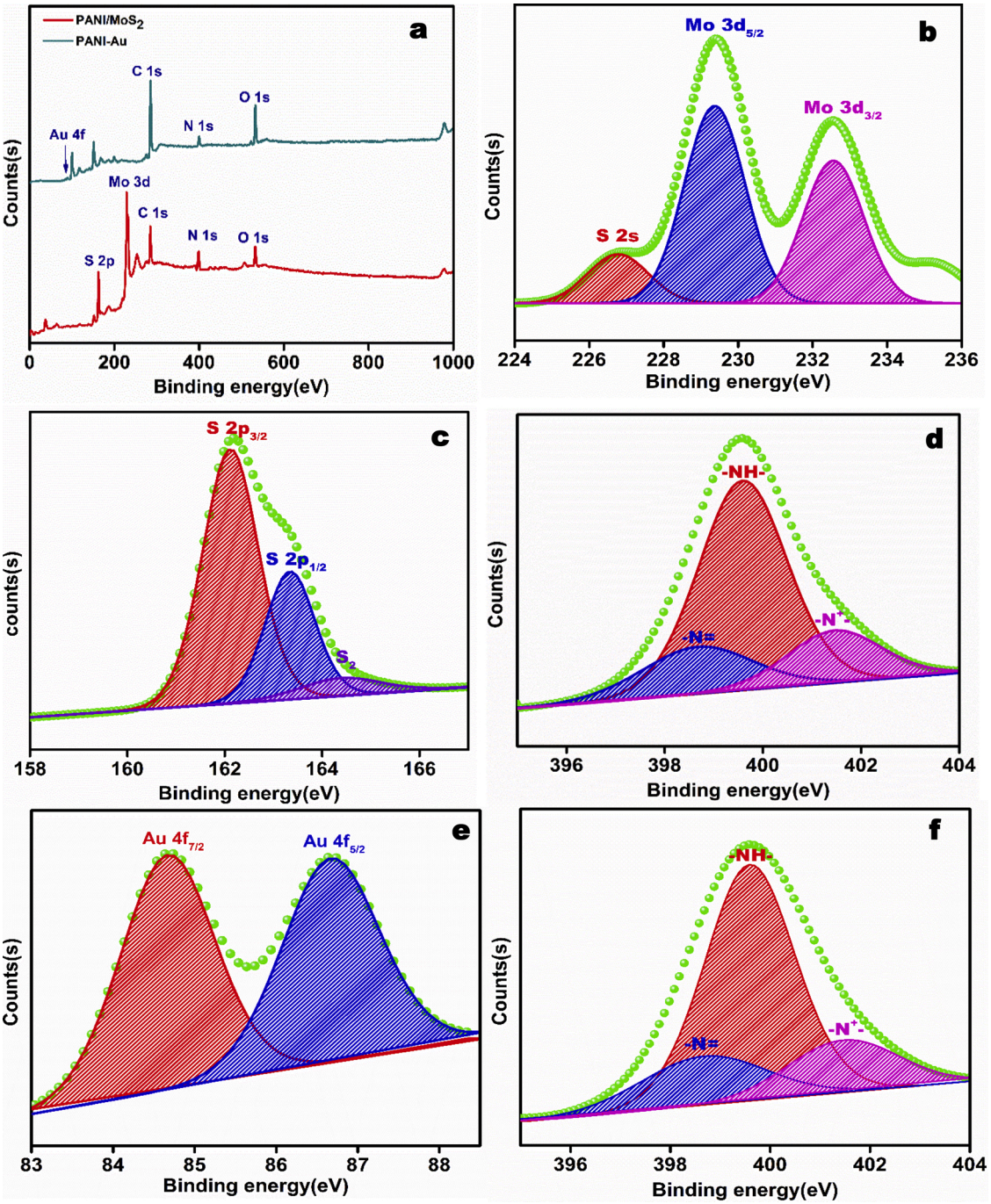


Fig. 2. XPS (a) full survey spectra of PANI/MoS_2 and PANI-Au, the deconvoluted spectrum of PANI/MoS_2 (b) Mo 3d, (c) S 2p, (d) N 1s, the deconvoluted spectrum of PANI-Au (e) Au 4f and (f) N 1s.

pattern no: 00-004-0784, Au (111), Au (200), Au (220), and Au (311) characteristic peaks corresponding to Au nanoparticles were observed at 38.2°, 44.4°, 64.7°, and 77.6°, respectively, which confirms the face-centered cubic structure of Au NPs; the highest peak intensity was observed at the Au (111) plane [44,45].

The elemental compositions of the PANI/MoS_2 and PANI-Au nanocomposites were investigated using X-ray photoelectron spectroscopy (XPS) analysis. The full survey spectrum shows coexistence of Mo, S, C, O, and N in PANI/MoS_2 and Au, C, O, and N elements in the PANI-Au nanocomposite (Fig. 2a). PANI/MoS_2 exhibited the Mo 3d, S 2p, C 1s, O 1s, and N 1s spectra; the expanded Mo 3d spectrum region contains S 2s, Mo $3d_{5/2}$, and Mo $3d_{3/2}$ (Fig. 2b). The S 2 s spectrum was captured at 226.7 eV, while the deconvoluted Mo $3d_{5/2}$ and Mo $3d_{3/2}$ peaks were recorded at 229.4 and 232.5 eV, respectively [46]. Deconvolution of the S 2p spectrum contains S $2p_{3/2}$, S $2p_{1/2}$, and S_2 peaks at 162.1, 163.3, and 164.2 eV, respectively [47] (Fig. 2c). Because of the presence of PANI in PANI/MoS_2, the C 1s deconvoluted region exhibited C-C/C-H and C-N peaks at 284.8 and 286.3 eV, respectively (Fig. S4a), and the N 1s deconvoluted spectrum displayed the presence of quinoid amine structure (-N=) (398.7 eV), benzenoid amine structure (-NH-) (399.6 eV), and a nitrogen cationic radical (-N^+-) (401.5 eV) [48](Fig. 2d). The PANI-Au nanocomposite contains Au 4f, C 1s, O 1s, and N 1s electronic oxidation states. In (Fig. 2e), the Au 4f deconvolution spectrum contains two peaks corresponding to Au $4f_{7/2}$ (84.7 eV) and Au $4f_{5/2}$ (86.7 eV) [49]. The C 1s spectrum of PANI-Au displayed C-C/C-H and C-N peaks at 285.0 and 286.8 eV, respectively (Fig. S4b). The deconvoluted N 1s peaks of PANI-Au could be attributed to the three nitrogen species, corresponding to (-N=) (398.6 eV), (-NH-) (399.6 eV), and (-N^+-) (401.6 eV) (Fig. 2f).

3.2. Electrochemical characterization of the PANI-Au-aCCP/BSA/CCP/PANI/MoS2/SPE immunosensor

3.2.1. Cyclic voltammetry

Prior aCCP detection, the electrochemical characteristics of the individual layers of the modified SPEs were investigated using cyclic voltammetry (CV) in the presence of 5 mM $Fe(CN)_6^{3-}/^{4-}$ in 0.1 M KCl. As can be observed from Fig. 3a, bare SPE generated a lower current (I_{pa} = 123.6 μA, I_{pc} = 104.1 μA) response due to its poor electrochemical behavior. A depletion of the electrochemical current (I_{pa} = 41.6 μA, I_{pc} = 34.0 μA) response was observed after the electrode surface was modified with MoS_2 ink. This is due to the formation of an electron-blocking layer between MoS_2/SPE and $Fe(CN)_6^{3-}/^{4-}$ ions at the electrode interface. PANI-modified electrodes shown an enhanced current response (I_{pa} = 703.8 μA, I_{pc} = 609.1 μA) because of a strong interaction between the amine functional group of PANI and $Fe(CN)_6^{3-}/^{4-}$. Because PANI was electropolymerized onto MoS_2/SPE, the electronegativity of MoS_2/SPE was completely neutralized, and it can be seen that high current (I_{pa} = 950.2 μA, I_{pc} = 838.5 μA) responses were captured for PANI/MoS_2/SPE. It can be concluded that the synergistic interaction effect between MoS_2

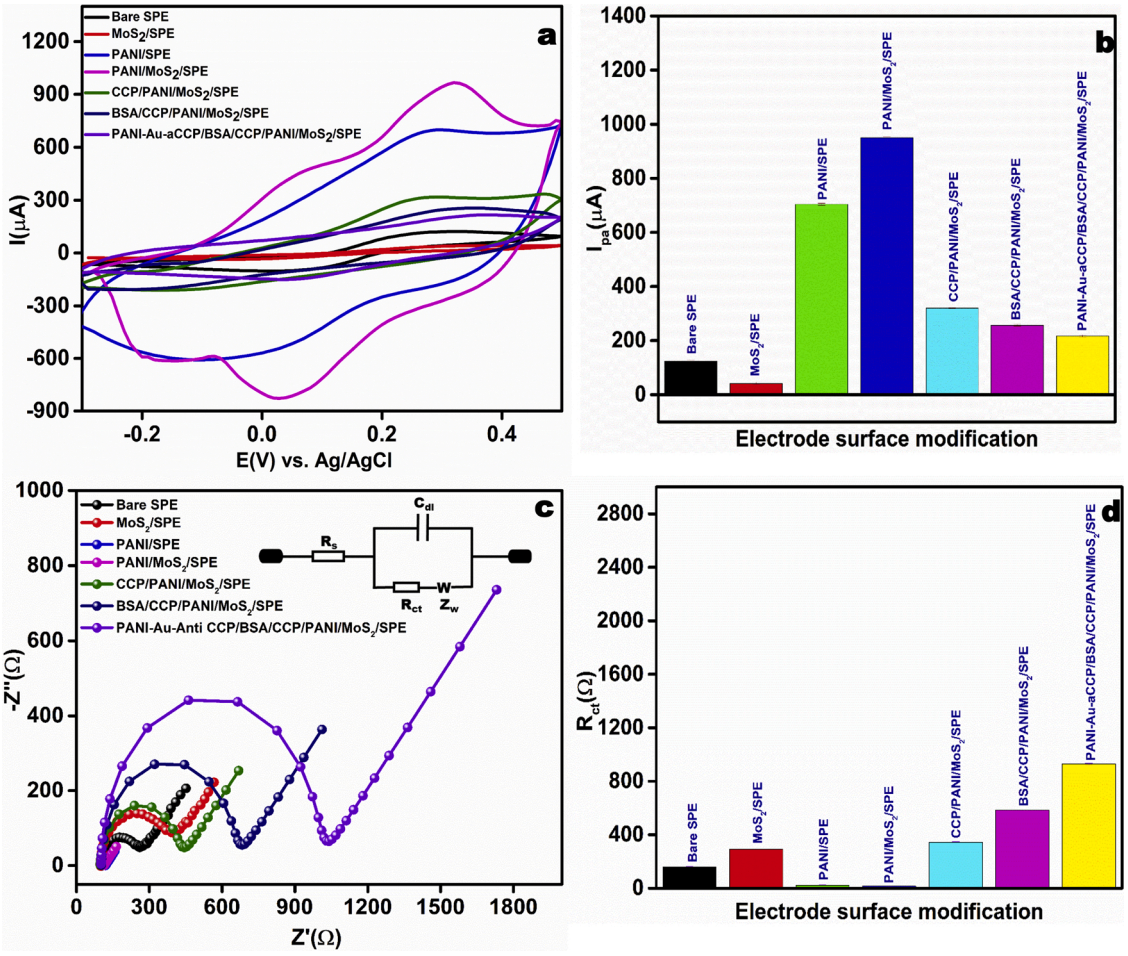


Fig. 3. (a) CV response of bare SPE, MoS_2/SPE, PANI/SPE, PANI/MoS_2/SPE, CCP/PANI/MoS_2/SPE, BSA/CCP/PANI/MoS_2/SPE, and PANI-Au-aCCP/BSA/CCP/PANI/MoS_2/SPE of different modified layers of SPE at 50 mV/s scan rate in 5 mM $Fe(CN)_6^{3-}/^{4-}$, (b) bar chart of different modified layers of aCCP immunosensor with their corresponding I_{pa} of CV response, (c) Nyquist plot of different modified layers of SPE: bare SPE, MoS_2/SPE, PANI/SPE, PANI/MoS_2/SPE, CCP/PANI/MoS_2/SPE, BSA/CCP/PANI/MoS_2/SPE, and PANI-Au-aCCP/BSA/CCP/PANI/MoS_2/SPE with a frequency range from 1 Hz to 1 MHz in 0.1 M KCl containing 5 mM $Fe(CN)_6^{3-}/^{4-}$, (d) bar chart of individual layers of aCCP immunosensor with their corresponding R_{ct} values.

and PANI caused a large increase in the electrochemical activity of PANI/MoS_2/SPE. Immobilization of CCP on PANI/MoS_2/SPE resulted in an insulating layer, which limited electron transfer, leading to an extreme decrease in the redox peak current (I_{pa} = 320.4 μA, I_{pc} = 208.6 μA). The remaining non-adsorptive sites of CCP/PANI/MoS_2/SPE were blocked upon immobilization of 0.5 % BSA; the CV response of BSA/CCP/PANI/MoS_2/SPE confirmed the decreased current response (I_{pa} = 256.8 μA, I_{pc} = 198.9 μA). Finally, upon addition of PANI-Au-aCCP, limited electron transfer (because of the affinity interaction between aCCP and CCP) generated a lower current response (I_{pa} = 216.9 μA, I_{pc} = 151.7 μA) (Scheme 1c). The importance of the entrapment of aCCP within PANI-Au was characterized by the CV response of aCCP/BSA/CCP/PANI/MoS_2/SPE, with and without the PANI-Au nanomatrix (Fig. S6). A depleted current response (I_{pa} = 95.8 μA, I_{pc} = 100.3 μA) was observed in the absence of PANI-Au. In contrast, when the aCCP antibodies-entrapped PANI-Au nanocomposite was added, enhanced current response (I_{pa} = 216.9 μA, I_{pc} = 151.7 μA) was observed because the high conductivity of the PANI-Au nanocomposite eased the detection of aCCP through SWV. The bar chart in Fig. 3b shows the changes in I_{pa} at each level of surface modification of the SPE. The complete results suggest that an aCCP immunosensor was developed successfully with a PANI-Au nanomatrix for entrapping aCCP antibodies using a BSA/CCPPANI/MoS_2 immunodetection platform.

3.2.2. *Electrochemical impedance spectroscopy*

The electrochemical charge transfer resistance (R_{ct}) contributions of the specific electrode layers, such as bare SPE, MoS_2/SPE, PANI/SPE, PANI/MoS_2/SPE, CCP/PANI/MoS_2/SPE, BSA/CCP/PANI/MoS_2/SPE, and PANI-Au-aCCP/BSA/CCP/PANI/MoS_2/SPE, were characterized using EIS Nyquist plots. The frequency was set between 1 Hz and 1 MHz and the obtained Nyquist plots were fitted through the best-fitting equivalent circuit. Charge transfer characteristics of the electrode surface are directed by the bulk solution resistance (R_s), double layer capacitance (C_{dl}) developed by ions at the electrode interface, charge transfer resistance (R_{ct}) because of the redox characteristic current flow at the electrode-electrolyte interface, and Z_w, which depicts the Warburg impedance. In Fig. 3c, the semicircle part of the Nyquist plot signifies the R_{ct} at the electrode interface and the linear section denotes the diffusion of electrons at the electrode surface. After fitting with an appropriate equivalent circuit, the obtained R_{ct} values for bare SPE, MoS_2/SPE, PANI/SPE, and PANI/MoS_2/SPE were found to be 159.1, 293.9, 20.6, and 15.6 Ω, respectively. As shown in Fig. 3c, bare SPE showed poor electrochemical response because of its lower electrochemical activity, while MoS_2/SPE showed that the electronegative charges accumulated at the surface of MoS_2/SPE instigated higher R_{ct}. The lowest R_{ct} was that of PANI/MoS_2/SPE (15.6 Ω), which signifies the high conductivity of the PANI/MoS_2-modified SPE. Successful immobilization of CCP was confirmed by the increased R_{ct} (342.1 Ω). The increased R_{ct} (582.1 Ω) at BSA/CCP/PANI/MoS_2/SPE confirmed the blocking of unbound CCP active sites at CCP/PANI/MoS_2/SPE to prevent nonspecific adsorption. Eventually, the highest R_{ct} (928.7 Ω) of PANI-Au-aCCP/BSA/CCP/PANI/MoS_2/SPE confirmed the interaction between aCCP and CCP, leading to the limited blocking of electron transfer at the electrode interface. The overall obtained results (Fig. 3d) suggest that the immunosensor for aCCP was successfully fabricated.

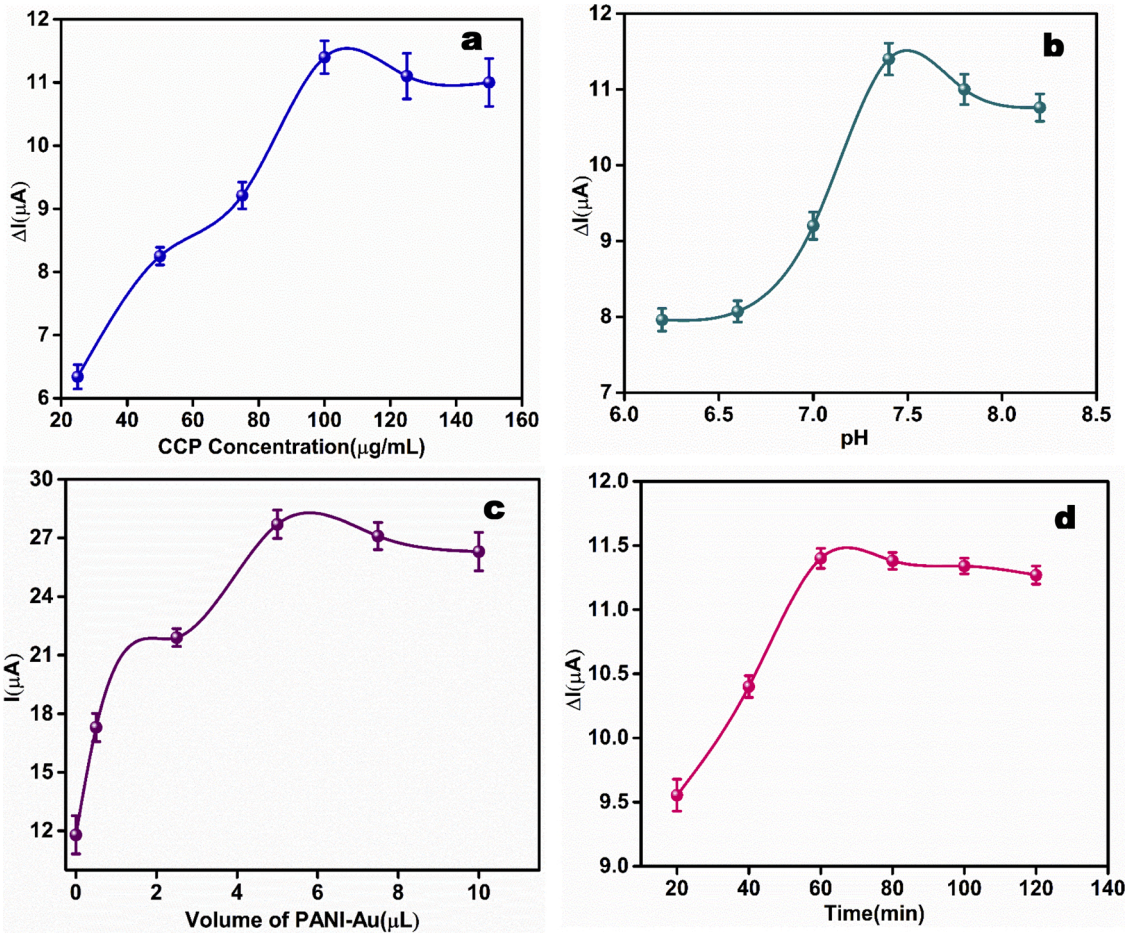


Fig. 4. Effect of (a) concentration of CCP, (b) pH, (c) loading volume of PANI-Au, and (d) incubation time on the catalytic current response of the developed aCCP immunosensor in the presence of 50.0 IU/mL of aCCP antibodies.

3.3. Optimization of the biosensor

Optimization of the experimental conditions is mandatory to enhance the performance of the immunosensor. First, varying concentrations (25.0–150.0 μg/mL) of CCP were tested against 50.0 IU/mL of the aCCP-attached PANI-Au nanomatrix in the developed immunosensor. From 25.0–100.0 μg/mL of CCP, the change in catalytic current response (ΔI) displayed a gradual increase, the highest ΔI was observed at 100.0 μg/mL of CCP, and from 125.0–150.0 μg/mL of CCP, the ΔI started to decline (Fig. 4a). Loading of CCP protein over 100 μg/mL at the confined electrode surface could be attributed to the aggregation of CCP where the blocking of citruline antibody binding site might tend to avoid the formation of CCP-aCCP immunocomplex upon the addition of PANI-Au-aCCP. Thus, the prohibition of CCP-aCCP immunocomplex formation might be ascribed to diminish the electron blocking layer (due to immunocomplex) of the confined electrode surface which led to the decrement of ΔI [50,51]. Thus, 100.0 μg/mL of CCP was chosen as the optimal concentration for the developed detection system. The ΔI of the developed aCCP immunosensor in the presence of 50.0 IU/mL of aCCP antibodies with PANI-Au at different pH levels (6.0–8.2). The ΔI increased gradually between pH 6.0 and 7.0 and attained maximum catalytic ΔI response at pH 7.4 (Fig. 4b). The biological activity between CCP and aCCP could be maintained with high affinity at near-neutral pH (7.4), which can be attributed to a high electrocatalytic current response. Thus, pH 7.4 was chosen as the optimal pH for the aCCP detection system. As aCCP antibodies could be adsorbed at the PANI-Au nanomatrix through electrostatic interactions between the aCCP antibodies and PANI-Au, the loading volume of PANI-Au plays a vital role in the performance of the detection system. The loading volume of the PANI-Au nanocomposite was studied between 0 and 10 μL (Fig. 4c). The SWV current response obtained with varying loading volumes of PANI-Au (0, 0.5, 2.5, 5.0, 7.5, and 10.0 μL) showed that 0–5.0 μL of PANI-Au enhanced the current response, 5.0 μL produced the maximum current response, and 7.5–10.0 μL of PANI-Au caused a decline in the current response because of steric hindrance at the electrode interface. To investigate the effect of incubation time on the electrochemical performance of the aCCP immunosensor, the immunosensor was evaluated in the presence of 50.0 IU/mL of aCCP with PANI-Au at different incubation times (0–90 min) (Fig. 4d). An obvious maximum SWV peak current change was observed at 60 min

3.4. SWV response characterization of the PANI-Au-aCCP/BSA/CCP/PANI/MoS_2/SPE immunosensor

Under augmented analytical conditions, the analytical performance of the BSA/CCP/PANI/MoS_2/SPE immunosensor was investigated using

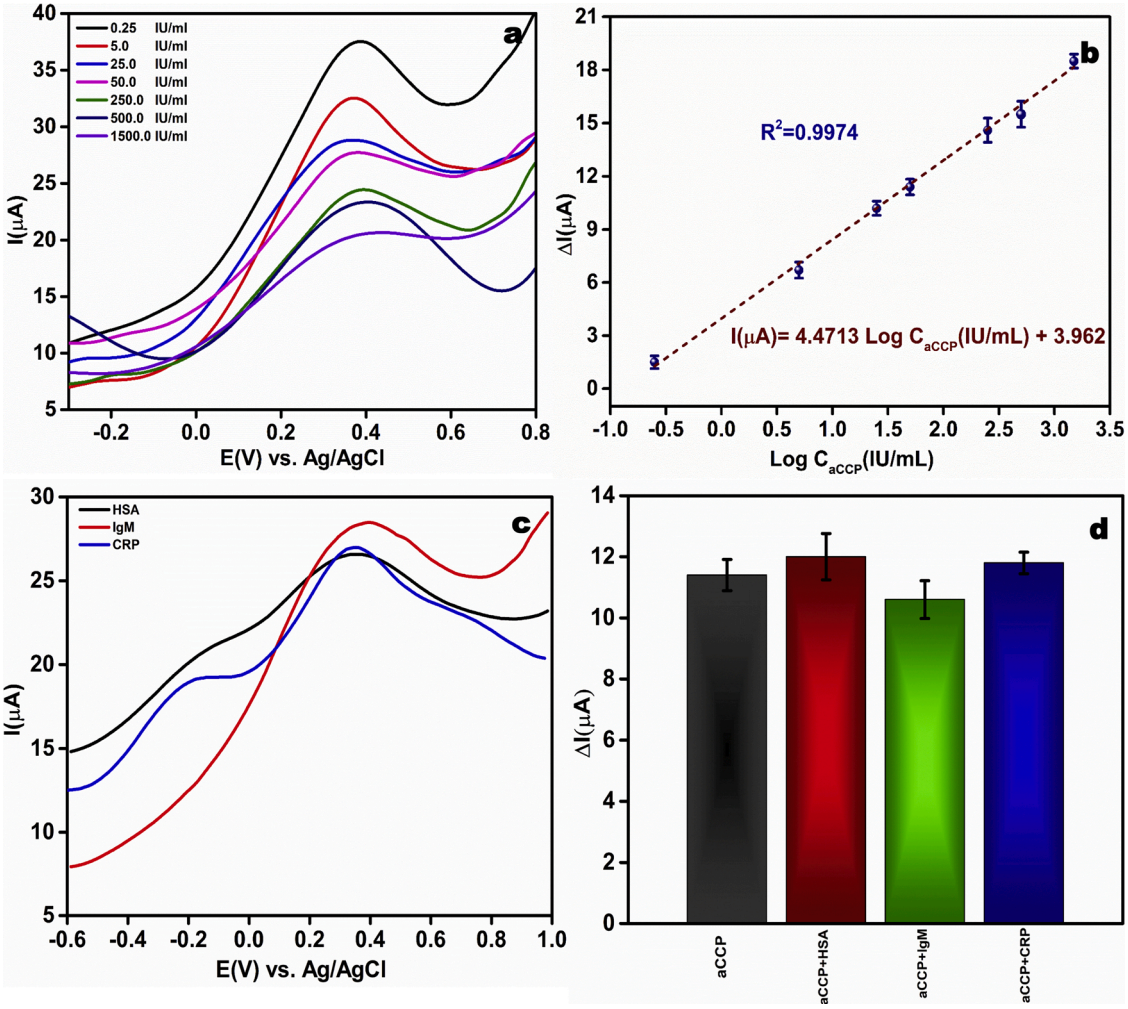


Fig. 5. (a) SWV response of BSA/CCP/PANI/MoS_2/SPE immunosensor using Au-PANI as a nanomatrix for the detection of different concentration of aCCP (0.25, 5.0. 25.0, 50.0, 250.0, 500.0, and 1,500.0 IU/mL) and (b) linear relationship between logarithmic concentration of aCCP *vs* current response obtained from SWV, (c) SWV response of 50.0 IU/mL of aCCP on BSA/CCP/PANI/MoS_2/SPE immunosensor using Au-PANI as a nanoprobe with interferents such as human serum albumin (HSA; 10 mg/mL), immunoglobulin M (IgM) RF (500 ng/mL), CRP (1,000 ng/mL), and (d) bar chart of change in current response in the presence and absence of interferents.

the SWV electroanalytical technique in the presence of 5 mM Fe $(CN)_6^{3-}/^{4-}$ as a redox mediator. The entire analytical investigation was carried out in the presence of 40 μL of electrolyte (1X PBS, pH = 7.4). After the successive addition of aCCP, the peak current response at 0.37 V decreased gradually, and the dynamic detection range of aCCP was analyzed (Fig. 5a). Variation in the peak current response of the developed sensor showed a linear relationship with the logarithmic concentration of aCCP from 0.25 to 1,500.0 IU/mL (Fig. 5b). ΔI represents the defined peak current decrement corresponding to aCCP concentration, which could be calculated from the following equation: $\Delta I = I_{no\ aCCP}$-I_{aCCP}, while $I_{no\ aCCP}$ is the peak current of the developed immunosensor without aCCP and I_{aCCP} corresponds to the peak current observed after addition of aCCP. The obtained equation was $\Delta I(\mu A) = 4.4713 \log C_{aCCP}(IU/mL)+3.962$ ($R^2 = 0.9974$) and the International Union of Pure and Applied Chemistry proposed standard method was employed to calculate the detection limit of the immunosensor. The LOD equation can be expressed as $LOD = 3S_D/S$ (S_D=standard deviation of 10 blanks without aCCP and S = slope of the calibration curve) [52]. Thus, the developed aCCP immunosensor detected aCCP antibodies in the logarithmic dynamic range of 0.25−1500 IU/mL with an LOD of 0.16 IU/mL (S/N = 3) in 1X PBS. Table S1 represents the higher detection limit and the broad range of linearity in the aCCP detection of current study across other reported literature. The higher detection limit of the immunosensor could be ascribed to the enhanced loading capacity of the aCCP antibodies on the PANI-Au nanomatrix. Furthermore, the enhanced electrocatalytic activity of the MoS_2/PANI SPE electrode base matrix caused a significant improvement in the electroanalytical performance of the developed sensor. The PANI base matrix was not only responsible for the enhanced electroanalytical performance but also aided the convenient immobilization of CCP on PANI/MoS_2/SPE through stable amide bond formation between CCP and PANI via EDC-NHS surface chemistry. The obtained experimental results suggest that the PANI/MoS_2 nanocomposite electrosensing base matrix and PANI-supported Au NP nanomatrix are potential candidates for a wide range of analytical dynamic ranges and higher detection limits.

3.5. Principle of the aCCP immunosensor

The aCCP immunosensor was developed based on BSA/CCP/PANI/MoS_2-modified SPE as a transducer base matrix with the employment of a PANI-Au nanocomposite to entrap the aCCP antibodies and enhance the electrochemical performance. Because of the presence of immobilized CCP on the surface-modified electrode, the CCP-immobilized SPE could recognize aCCP antibodies with a higher degree of affinity (Scheme 1b). In the absence of aCCP antibodies, a higher SWV response was obtained, while in the presence of aCCP antibodies, a reduction in the current response was observed with $Fe(CN)_6^{3-}/^{4-}$ as a redox probe. For this immunological biosensor, the transducing mechanism was defined based on decrement in the SWV current response because of formation of the CCP-aCCP immunocomplex, which caused limited electron transfer at the electrode interface (Scheme 1b). As the PANI-Au-aCCP/BSA/CCP/PANI/MoS_2/SPE was completely insulated using 0.5 % BSA, the changes in the current response completely relied on the aCCP concentration.

3.6. Practical application of the biosensor

3.6.1. Interference study

The interference study of the aCCP immunosensor was established by verifying the SWV response of the developed sensor in the presence of 50.0 IU/mL aCCP antibodies against the specific coexisting proteins in the serum samples. Thus, human serum albumin (HSA; 10 mg/mL), immunoglobulin M (IgM) RF (100 ng/mL), CRP ab (inflammatory antibody) (1,000 ng/mL), and were tested against aCCP (50 IU/mL). According to the optimized condition, having interferents added, the assay was incubated for 60 min at 4 °C and then washed with 40 μL of 1X PBS twice then, in the presence of 5 mM $Fe(CN)_6^{3-}/^{4-}$ in 1X PBS (pH = 7.4), SWV study was conducted. Fig. 5c displays the recorded SWV response of 50.0 IU/mL of aCCP on BSA/CCP/PANI/MoS_2/SPE using PANI-Au as a constructed nanomatrix for entrapping aCCP with the abovementioned interferents. The bar chart (Fig. 5d) of the SWV response revealed that there was no noteworthy deviation in the current response (ΔI); in addition, the obtained % relative standard deviation (RSD) was 4.67 %, which is less than 5%. The error bar signifies the aCCP current response of three independent measurements (n = 3). Thus, the developed aCCP immunosensor can detect aCCP antibodies with high selectivity.

3.6.2. Stability and precision

The storage stability of the developed aCCP immunosensor was evaluated by measuring its performance after storage for 4 weeks at 4 °C. The study was conducted and the SWV responses were recorded in the presence of 50.0 IU/mL of aCCP (Fig. 6a). The sensor retained 92.3 % of its initial peak current after 4 weeks. Moreover, the calculated % RSD of ΔI was 2.92 %, which is less than 5%. Thus, the developed aCCP immunosensor can be stored for 21 days (3 weeks) and still produce exceptionally efficient results. The reproducibility of aCCP detection was carried out in the presence of 50.0 IU/mL of aCCP on the developed immunosensor. Fig. 6b displays the obtained SWV response for 50.0 IU/mL of aCCP on five different electrodes; the bar chart depicts the five different electrodes and their corresponding ΔI values (Fig. 6c). The standard deviation of three different measurements has been denoted as error bars (n = 3), while the calculated %RSD of the reproducibility was found to be 3.32 %. Repeatability measurements were taken on the same electrode for eight different measurements, and the calculated %RSD of intra-assay was found to be 3.49 %.

3.6.3. Real-time analysis in human serum samples

The sensor was applied to aCCP antibody-spiked human serum samples to investigate the real-time application of the developed sensor under optimized conditions. The abundance of refitting the equation in the real-time analysis is because to eliminate the matrix effect and to construct the robust calibration plot which could be the main factor in higher specificity towards aCCP antibodies in serum samples. Because of the complexity of human serum, the serum sample was diluted to 10 % (V/V) with 1X PBS (pH = 7.4) [1,11]. However, before analyzing the aCCP antibody-spiked serum samples, the SWV reading of diluted [10 % (V/V)] serum was recorded and considered as a blank value. aCCP antibody-spiked (0.25, 1.0, 10.0, 100.0, 500.0, 1,000.0, and 1500.0 IU/mL) serum samples were analyzed under optimized conditions with 5 mM $Fe(CN)_6^{3-}/^{4-}$ as a redox probe in 1X PBS. The recorded SWV readings of serum samples spiked with aCCP antibodies were subtracted from the blank value to eliminate the matrix effect of human serum. The recorded SWV responses have been plotted in Fig. 7a and it was observed that increasing the concentration of aCCP gradually decreased the current response at 0.29 V. The principle of the developed immunosensor on human serum followed the same mechanism and trend as that observed in 1X PBS (Fig. 7a). However, the oxidation potential shifted slightly toward the negative side due to the matrix effect in human serum. The obtained SWV peak currents were subtracted from the peak current of 10 % human serum, the calculated values for which have been plotted in Fig. 7b. The linearity equation of $\log C_{HS\text{-}aCCP}$ *vs* ΔI can be expressed as $\Delta I\ (\mu A) = 2.8695 \log C_{HS\text{-}aCCP}\ (IU/mL)+2.1503$ ($R^2 = 0.9944$), where the error bar denotes the standard deviation of three independent measurements and the calculated LOD of aCCP detection in aCCP-spiked human serum was 0.22 IU/mL, with a logarithmic dynamic linear range between 0.25−1500 IU/mL (S/N = 3). Moreover, the dynamic range of aCCP antibodies detection between 2.5–15000 IU/mL in 100 % serum would match the actual aCCP antibodies concentration in human serum, as the concentration of aCCP increases 1000 folds with the progression of chronic inflammation in RA patients. Comparison of the aCCP immunosensor performance in 1X PBS and 10 % HS were

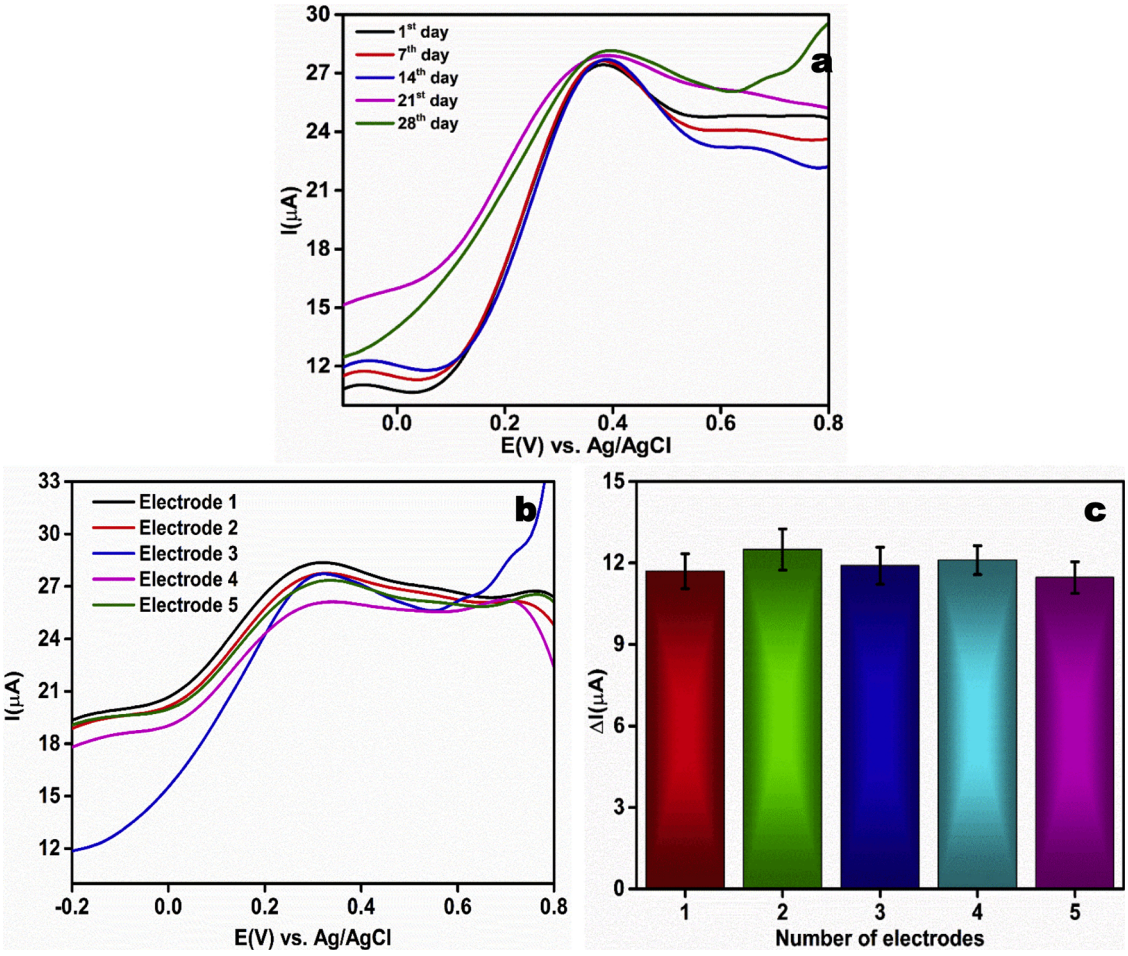


Fig. 6. (a) Four-week storage (at 4 °C) stability study of the developed aCCP immunosensor in the presence of 50.0 IU/mL aCCP, (b) SWV response of five different Au-PANI/aCCP/BSA/CCP/BSA/CCP/PANI/MoS_2/SPE immunosenosors in the presence of 50.0 IU/mL of anti-CCP and 5 mM $Fe(CN)_6^{3-/4-}$ as a redox probe and (c) bar chart represents SWV current response of five different electrodes. Error bars indicate the standard deviation of three independent measurements (n = 3).

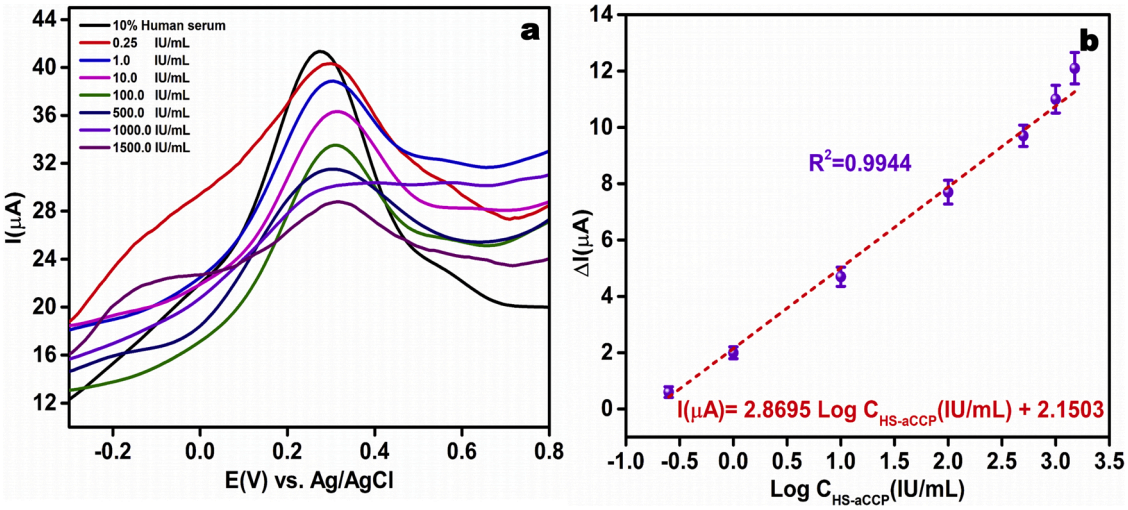


Fig. 7. (a) SWV response of BSA/CCP/PANI/MoS_2/SPE immunosensor using Au-PANI as a nanoprobe for the detection of anti-CCP spiked human serum (0.25, 1.0. 10.0, 100.0, 500.0, 1000.0, and 1,500.0 IU/mL) and (b) Linear relationship between log $C_{HS\text{-}aCCP}$ *vs* change in current response.

tabulated in Table 1. Because of the matrix effect in human serum, change in the immunosensor performance between 1X PBS and 10 % HS was observed. To nullify the matrix effect, refitting of real-time calibration plot of 10 % HS was constructed for the accurate measurement of aCCP antibodies [1].

Table 1
Performance of aCCP sensor parameters.

Sensor parameters	1X PBS	10 % HS
Log linear range (IU/mL)	0.25−1500 IU/mL	0.25−1500 IU/mL
Slope of calibration curve	4.4713	2.8695
SD of blanks	0.2394	0.2132
LOD (IU/mL)	0.1607	0.2229

4. Conclusion

In this work, probe-sonicated MoS_2 nanosheets containing ink were drop-casted on SPE to fabricate the electrode base matrix and a fine layer of PANI was electrodeposited on MoS_2/SPE. Precise immobilization of CCP was performed on PANI/MoS_2/SPE using EDC-NHS surface chemistry. A PANI-Au nanomatrix, was employed to enhance the loading amount of aCCP antibodies which improves the sensitivity of the aCCP immunosensor. Upon applying the BSA/CCP/PANI/MoS_2/SPE-based immunosensor, aCCP detection was carried out in 1X PBS with an LOD of 0.16 IU/mL and in 10 % human serum 0.22 IU/mL of detection limit was observed with a logarithmic dynamic range from 0.25–1500.0 IU/mL. Furthermore, the aCCP immunosensor was able to distinguish aCCP from other human serum proteins and showed excellent selectivity because of the immobilization of CCP. The aCCP immunosensor could be stored at 4^{o}C with limited storage stability for 3 weeks. The total time required for aCCP detection was found to be within 2 h, which includes the immobilization of CCP and the final addition of PANI-Au-aCCP. The developed sensor displays advantages over other reported works, such as a simple detection protocol and a smaller sample volume of 10 μL, which is 10 times less volume than that required for commercial ELISA kits.

CRediT authorship contribution statement

Sathish Panneer Selvam: Conceptualization, Methodology, Formal analysis, Validation, Investigation, Writing - original draft. **Somasekhar R. Chinnadayyala:** Conceptualization, Formal analysis, Data curation, Validation, Writing - review & editing. **Sungbo Cho:** Resources, Writing - review & editing, Supervision, Project administration, Funding acquisition.

Declaration of Competing Interest

The authors report no declarations of interest.

Acknowledgements

This research was supported by the National Research Foundation of Korea (NRF) (grant nos. NRF-2019R1A2C1088680, 2018M3A9F1023691, 2020M3A9E410438511). We are thankful to Arun Samuel Pandian for his immense support in designing the graphical visualization of this study.

Appendix A. Supplementary data

Supplementary material related to this article can be found, in the online version, at doi:https://doi.org/10.1016/j.snb.2021.129570.

References

[1] S.R. Chinnadayyala, J. Park, M.A. Abbasi, S. Cho, Label-free electrochemical impedimetric immunosensor for sensitive detection of IgM rheumatoid factor in human serum, Biosens. Bioelectron. 143 (2019), 111642.
[2] E. Myasoedova, C.S. Crowson, H.M. Kremers, T.M. Therneau, S.E. Gabriel, Is the incidence of rheumatoid arthritis rising? Results from Olmsted County, Minnesota, 1955-2007, Arthritis Rheum. 62 (2010) 1576–1582.
[3] R. Samanta, K. Shoukrey, R. Griffiths, Rheumatoid arthritis and anaesthesia, Anaesthesia 66 (2011) 1146–1159.
[4] L. Fugger, A. Svejgaard, Association of MHC and rheumatoid arthritis HLA-DR4 and rheumatoid arthritis: studies in mice and men, Arthritis Res. 2 (2000) 208–211.
[5] P.K. Gregersen, J. Silver, R.J. Winchester, The shared epitope hypothesis, Arthritis Rheum. 30 (1987) 1205–1212.
[6] Y.T. Ting, J. Petersen, S.H. Ramarathinam, S.W. Scally, K.L. Loh, R. Thomas, A. Suri, D.G. Baker, A.W. Purcell, H.H. Reid, J. Rossjohn, The interplay between citrullination and HLA-DRB1 polymorphism in shaping peptide binding hierarchies in rheumatoid arthritis, J. Biol. Chem. 293 (2018) 3236–3251.
[7] M.M.J. Nielen, D. Van Schaardenburg, H.W. Reesink, R.J. Van De Stadt, I.E. Van Der Horst-Bruinsma, M.H.M.T. De Koning, M.R. Habibuw, J.P. Vandenbroucke, B. A.C. Dijkmans, Specific autoantibodies precede the symptoms of rheumatoid arthritis: a study of serial measurements in blood donors, Arthritis Rheum. 50 (2004) 380–386.
[8] L.M. Enriconi dos Anjos, I.A. Pereira, E. d' Orsi, A.P. Seaman, R.W. Burlingame, E. F. Morato, A comparative study of IgG second- and third-generation anti-cyclic citrullinated peptide (CCP) ELISAs and their combination with IgA third-generation CCP ELISA for the diagnosis of rheumatoid arthritis, Clin. Rheumatol. 28 (2009) 153–158.
[9] I. Alexiou, A. Germenis, A. Ziogas, K. Theodoridou, L.I. Sakkas, Diagnostic value of anti-cyclic citrullinated peptide antibodies in Greek patients with rheumatoid arthritis, BMC Musculoskelet. Disord. 8 (2007) 1–7.
[10] Y. Wang, F. Pei, X. Wang, Z. Sun, C. Hu, H. Dou, Meta-analysis: diagnostic accuracy of anti-cyclic citrullinated peptide antibody for juvenile idiopathic arthritis, J. Immunol. Res. (2015) (2015).
[11] S. Guerrero, E. Sánchez-Tirado, G. Martínez-García, A. González-Cortés, P. Yáñez-Sedeño, J.M. Pingarrón, Electrochemical biosensor for the simultaneous determination of rheumatoid factor and anti-cyclic citrullinated peptide antibodies in human serum, Analyst 145 (2020) 4680–4687.
[12] R. Aggarwal, K. Liao, R. Nair, S. Ringold, K.H. Costenbader, Anti-citrullinated peptide antibody assays and their role in the diagnosis of rheumatoid arthritis, Arthritis Care Res. 61 (2009) 1472–1483.
[13] R. Elshafey, M. Siaj, A.C. Tavares, Au nanoparticle decorated graphene nanosheets for electrochemical immunosensing of p53 antibodies for cancer prognosis, Analyst 141 (2016) 2733–2740.
[14] T.D. Jaskowski, H.R. Hill, K.L. Russo, G. Lakos, Z. Szekanecz, M. Teodorescu, Relationship between rheumatoid factor isotypes and IgG anti-cyclic citrullinated peptide antibodies, J. Rheumatol. 37 (2010) 1582–1588.
[15] H. Chon, S. Lee, R. Wang, S.Y. Bang, H.S. Lee, S.C. Bae, H. Lee, B. Kim, J. Choo, SERS-based immunoassay of anti-cyclic citrullinated peptide for early diagnosis of rheumatoid arthritis, RSC Adv. 4 (2014) 32924–32927.
[16] H. Chon, S. Lee, R. Wang, S.-Y. Bang, H.-S. Lee, S.-C. Bae, S.H. Hong, Y.H. Yoon, D. Lim, J. Choo, Highly sensitive immunoassay of anti-cyclic citrullinated peptide marker using surface-enhanced Raman scattering detection, Int. Conf. Nano-Bio Sensing Imaging Spectrosc. 9523 (2015) (2015) 95230J.
[17] R. Tanaka, M. Takemura, M. Sato, Y. Yamada, T. Nakagawa, T. Horibe, M. Hoshi, H. Otaki, H. Ito, M. Seishima, K. Shimizu, Comparison of chemiluminescence enzyme immunoassay (CLEIA) with ELISA for the determination of anti-cyclic citrullinated peptide antibodies, Clin. Chim. Acta 411 (2010) 22–25.
[18] S.M. Hwang, J.O. Kim, Y.M. Yoo, S. Shin, J.Q. Kim, M.H. Park, E.Y. Song, Performance analysis of the ARCHITECT anti-cyclic citrullinated peptide antibody in the diagnosis of rheumatoid arthritis, Clin. Chem. Lab. Med. 48 (2010) 225–230.
[19] H. Ko, G. yeon Lee, B.J. Jeon, J.C. Pyun, Fluorescence immunoassay of anti-cyclic citrulinated peptide (CCP) autoantibodies by using parylene-H film, Biochip J. 5 (2011) 242–245.
[20] R.C.B. Marques, E. Costa-Rama, S. Viswanathan, H.P.A. Nouws, A. Costa-García, C. Delerue-Matos, M.B. González-García, Voltammetric immunosensor for the simultaneous analysis of the breast cancer biomarkers CA 15-3 and HER2-ECD, Sens. Actuators B Chem. 255 (2018) 918–925.
[21] H. Yan, L. Gong, L. Zang, H. Dai, G. Xu, S. Zhang, Y. Lin, Dual-responsive competitive immunosensor for sensitive detection of tumor marker on g-CN/rGO conjugation, Sens. Actuators B Chem. 230 (2016) 810–817.
[22] J. Wang, D. Yang, M. Chen, B. Liu, H. Chen, H. Xu, W. Wang, L. Bai, Electrochemical immunosensor detection of tumor markers based on a GO composite nanoprobe for signal amplification, Anal. Methods 10 (2018) 526–532.
[23] Y. Li, L. Liu, X. Liu, Y. Ren, K. Xu, N. Zhang, X. Sun, X. Yang, X. Ren, Q. Wei, A dual-mode PCT electrochemical immunosensor with $CuCo_2S_4$ bimetallic sulfides as enhancer, Biosens. Bioelectron. 163 (2020), 112280.
[24] J. Yao, Y. Wang, Y. Dai, C.C. Liu, Bioconjugated, single-use biosensor for the detection of biomarkers of prostate cancer, ACS Omega 3 (2018) 6411–6418.
[25] D.M.N. Luna, K.Y.P.S. Avelino, M.T. Cordeiro, C.A.S. Andrade, M.D.L. Oliveira, Electrochemical immunosensor for dengue virus serotypes based on 4-mercapto-benzoic acid modified gold nanoparticles on self-assembled cysteine monolayers, Sens. Actuators B Chem. 220 (2015) 565–572.
[26] S. Khetani, V. Ozhukil Kollath, V. Kundra, M.D. Nguyen, C. Debert, A. Sen, K. Karan, A. Sanati-Nezhad, Polyethylenimine modified graphene-oxide electrochemical immunosensor for the detection of glial fibrillary acidic protein in central nervous system injury, ACS Sens. 3 (2018) 844–851.
[27] F. Li, J. Feng, Z. Gao, L. Shi, D. Wu, B. Du, Q. Wei, Facile synthesis of Cu_2O@TiO_2-PtCu nanocomposites as a signal amplification strategy for the insulin detection, ACS appl, Mater. Interfaces. 11 (2019) 8945–8953.
[28] J. Yukird, T. Wongtangprasert, R. Rangkupan, O. Chailapakul, T. Pisitkun, N. Rodthongkum, Label-free immunosensor based on graphene/polyaniline nanocomposite for neutrophil gelatinase-associated lipocalin detection, Biosens. Bioelectron. 87 (2017) 249–255.

[29] X. Mo, Z. Wu, J. Huang, G. Zhao, W. Dou, A sensitive and regenerative electrochemical immunosensor for quantitative detection of: escherichia coli O157: H7 based on stable polyaniline coated screen-printed carbon electrode and rGO-NR-Au@Pt, Anal. Methods 11 (2019) 1475–1482.
[30] U.Z.M. Azmi, N.A. Yusof, N. Kusnin, J. Abdullah, S. Suraiya, P.S. Ong, N.H. A. Raston, S.F.A. Rahman, M.F.M. Fathil, Sandwich electrochemical immunosensor for early detection of tuberculosis based on graphene/polyaniline-modified screen-printed gold electrode, Sensors (Switzerland) 18 (2018) 1–14.
[31] X. Li, M. Yu, Z. Chen, X. Lin, Q. Wu, A sensor for detection of carcinoembryonic antigen based on the polyaniline-Au nanoparticles and gap-based interdigitated electrode, Sens. Actuators B Chem. 239 (2017) 874–882.
[32] O. Parlak, A. İncel, L. Uzun, A.P.F. Turner, A. Tiwari, Structuring Au nanoparticles on two-dimensional MoS_2 nanosheets for electrochemical glucose biosensors, Biosens. Bioelectron. 89 (2017) 545–550.
[33] K.J. Huang, J.Z. Zhang, Y.J. Liu, L.L. Wang, Novel electrochemical sensing platform based on molybdenum disulfide nanosheets-polyaniline composites and Au nanoparticles, Sens. Actuators B Chem. 194 (2014) 303–310.
[34] G. Maduraiveeran, M. Sasidharan, V. Ganesan, Electrochemical sensor and biosensor platforms based on advanced nanomaterials for biological and biomedical applications, Biosens. Bioelectron. 103 (2018) 113–129.
[35] R. Gangopadhyay, A.D. Chowdhury, A. De, Functionalized polyaniline nanowires for biosensing, Sens. Actuators B Chem. 171–172 (2012) 777–785.
[36] A. Ganguly, J. Benson, P. Papakonstantinou, Sensitive chronocoulometric detection of miRNA at screen-printed electrodes modified by gold-decorated MoS_2 nanosheets, ACS Appl. Bio Mater. 1 (2018) 1184–1194.
[37] A.K. Yagati, S.G. Chavan, C. Baek, M.H. Lee, J. Min, Label-free impedance sensing of aflatoxin B1 with polyaniline nanofibers/Au nanoparticle electrode array, Sensors (Switzerland) 18 (2018) 1–14.
[38] J. Bart, R. Tiggelaar, M. Yang, S. Schlautmann, H. Zuilhof, H. Gardeniers, Room-temperature intermediate layer bonding for microfluidic devices, Lab Chip 9 (2009) 3481–3488.
[39] R.V. Kashid, D.J. Late, S.S. Chou, Y.K. Huang, M. De, D.S. Joag, M.A. More, V. P. Dravid, Enhanced field-emission behavior of layered MoS_2 sheets, Small 9 (2013) 2730–2734.
[40] C.P. Veeramalai, F. Li, Y. Liu, Z. Xu, T. Guo, T.W. Kim, Enhanced field emission properties of molybdenum disulphide few layer nanosheets synthesized by hydrothermal method, Appl. Surf. Sci. 389 (2016) 1017–1022.
[41] K.W. Song, M.H. Park, T.H. Kim, S.H. Lim, C.W. Yang, UV enhanced synthesis of high density Au coated ZnO nanocomposite, J. Nanosci. Nanotechnol. 14 (2014) 8766–8770.
[42] B.L. Li, H.Q. Luo, J.L. Lei, N.B. Li, Hemin-functionalized MoS_2 nanosheets: enhanced peroxidase-like catalytic activity with a steady state in aqueous solution, RSC Adv. 4 (2014) 24256–24262.
[43] H. Xu, J. Zhang, Y. Chen, H. Lu, J. Zhuang, Electrochemical polymerization of polyaniline doped with Cu^{2+} as the electrode material for electrochemical supercapacitors, RSC Adv. 4 (2014) 5547–5552.
[44] T.T. Vo, C.H. Dang, V.D. Doan, V.S. Dang, T.D. Nguyen, Biogenic synthesis of silver and gold nanoparticles from Lactuca indica leaf extract and their application in catalytic degradation of toxic compounds, J. Inorg. Organomet. Polym. Mater. 30 (2020) 388–399.
[45] V.D. Doan, B.A. Huynh, T.D. Nguyen, X.T. Cao, V.C. Nguyen, T.L.H. Nguyen, H. T. Nguyen, V.T. Le, Biosynthesis of silver and gold nanoparticles using aqueous extract of Codonopsis pilosula roots for antibacterial and catalytic applications, J. Nanomater. (2020) (2020).
[46] B. Li, L. Jiang, X. Li, P. Ran, P. Zuo, A. Wang, L. Qu, Y. Zhao, Z. Cheng, Y. Lu, Preparation of monolayer MoS_2 quantum dots using temporally shaped femtosecond laser ablation of bulk MoS_2 targets in water, Sci. Rep. 7 (2017) 1–12.
[47] L. Zhao, J. Jia, Z. Yang, J. Yu, A. Wang, Y. Sang, W. Zhou, H. Liu, One-step synthesis of CdS nanoparticles/MoS_2 nanosheets heterostructure on porous molybdenum sheet for enhanced photocatalytic H_2 evolution, Appl. Catal. B Environ. 210 (2017) 290–296.
[48] P. Ahuja, S.K. Ujjain, I. Arora, M. Samim, Hierarchically grown NiO-Decorated polyaniline-reduced graphene oxide composite for ultrafast sunlight-driven photocatalysis, ACS Omega 3 (2018) 7846–7855.
[49] M. Sharifuzzaman, S.C. Barman, M.A. Zahed, N.J. San, J.Y. Park, Green synthesis of reduced graphene oxide decorated with few-layered MoS_2-nanoroses and Au/Pd/Ag trimetallic nanoparticles for ultrasensitive label-free immunosensing platforms, J. Electrochem. Soc. 166 (2019) B249–B257.
[50] Y. Shen, G. Shen, Electrochemical impedimetric immunosensor based on host–guest interaction between β-cyclodextrin and ferrocene anchored to ionic liquid, Ionics (Kiel) 25 (2019) 3407–3412.
[51] Y. Wang, S. Sun, J. Luo, Y. Xiong, T. Ming, J. Liu, Y. Ma, S. Yan, Y. Yang, Z. Yang, J. Reboud, H. Yin, J.M. Cooper, X. Cai, Low sample volume origami-paper-based graphene-modified aptasensors for label-free electrochemical detection of cancer biomarker-EGFR, Microsyst. Nanoeng. 6 (2020) 32.
[52] O. da Silva, S.A.S. Machado, Evaluation of the detection and quantification limits in electroanalysis using two popular methods: application in the case study of paraquat determination, Anal. Methods 4 (2012) 2348–2354.

Sathish Panneer Selvam is a PhD student in the Department of Electronics engineering, Gachon University, Gyeonggi-do, Republic of Korea. Currently, he is working on electrochemistry, nanomaterial-based electrochemical sensors, functionalized nanomaterials and immunosensors.

Dr. Somasekhar R. Chinnadayyala received his M.Sc. degree in Bio-chemistry from YogiVemana University, India, in 2008 and a PhD degree from Indian institute of technology, Guwahati, India, in 2015 in the area of Biosciences and Bioengineering. From 2016–2017, he was a post-doctoral scientist in Department of Chemistry at Soongsil University, Seoul, Republic of Korea. He is currently working as an assistant professor in the Department of electronics engineering, Gachon university, Seongnam, Republic of Korea. His research interests include the development of affinity based impedimetric biosensors, enzyme/non-enzyme-based electrochemical nano-biosensors for clinical diagnosis.

Prof. Sungbo Cho received his B.S. and M.S. in Electrical engineering at Korea University in 2001, Seoul, Republic of Korea and Dr.-Ing. degree in Physics and Mechatronics at Saarland University/Fraunhofer Institute for Biomedical Engineering (FhG-IBMT), Saarbruecken, Germany in 2008. Prof. Sungbo Cho is an Associate Professor of the Electronic Engineering at Gachon University, Seongnam, Korea. His interest has been focused on the development of electrical impedimetric biosensors.